Heliyon 10 (2024) e41089

Contents lists available at ScienceDirect

Heliyon

journal homepage: www.cell.com/heliyon

Research article

Fabricating ZnO@C composites based on *Nypa fruticants* shell-derived cellulose for high performance lithium-ion battery anodes

Quang Quoc Viet Thieu [a,b], Thi Hoang Thy Tran [a], Hai Dang Ngo [c], Liem Thanh Pham [d,e], Man Van Tran [d,e,f], Ngoc Quang Tran [g,e], Nguyen Phuc Thien Le [h,e], Dinh Quan Nguyen [h,e], Tuan Loi Nguyen [i,j,*], Il Tae Kim [k,**]

[a] *Composite Materials Lab, College of Engineering, Can Tho University, Viet Nam*
[b] *Faculty of Chemical Engineering, College of Engineering, Can Tho University, Campus II, 3/2 Street, Ninh Kieu District, Can Tho City, Viet Nam*
[c] *Faculty of Applied Sciences, Ho Chi Minh City University of Technology and Education (HCMUTE), Thu Duc City, Ho Chi Minh City, Viet Nam*
[d] *Applied Physical Chemistry Laboratory (APCLAB), VNUHCM-University of Science, Viet Nam*
[e] *Vietnam National University Ho Chi Minh City, Linh Trung Ward, Thu Duc City, Ho Chi Minh City, Viet Nam*
[f] *Department of Physical Chemistry, Faculty of Chemistry, VNUHCM-University of Science, Viet Nam*
[g] *Center for Innovative Materials and Architectures, Ho Chi Minh City, 700000, Viet Nam*
[h] *Laboratory of Biofuel and Biomass Research, Faculty of Chemical Engineering, Ho Chi Minh City University of Technology (HCMUT), 268 Ly Thuong Kiet Street, District 10, Ho Chi Minh City, Viet Nam*
[i] *Institute of Fundamental and Applied Sciences, Duy Tan University, Ho Chi Minh City, 70000, Viet Nam*
[j] *Faculty of Environmental and Chemical Engineering, Duy Tan University, Da Nang City, 50000, Viet Nam*
[k] *Department of Chemical, Biological & Battery Engineering, Gachon University, Seongnam-si, Gyeonggi-do, 13120, Republic of Korea*

ARTICLE INFO

Keywords:
Lithium-ion batteries
Nypa fruticants shell
Composite materials
Zinc oxide
Biomass waste

ABSTRACT

In this study, *Nypa fruticans* shell-derived cellulose was successfully produced, and the hydrothermal method was employed to generate ZnO@C (ZOC) composites, which were then subjected to calcination in N_2 gas at a temperature of 600 °C for varying durations. X-ray diffraction and thermogravimetric analyses demonstrated that the annealing duration had a substantial impact on the quantities of C and ZnO in the ZOC composites. The scanning electron microscope images indicated the presence of ZnO nanoparticles on the surface of the C phase and revealed a similar morphology among the ZOC composites. ZOC anodes exhibited excellent electrochemical properties when used in lithium-ion batteries (LIBs), making them promising alternatives to graphite as LIB anode materials. As an illustration, the ZOC_2h electrode delivered a reversible capacity of 500 mAh g^{-1} after 100 cycles at a current density of 0.1 A g^{-1}. The excellent electrochemical performance of the ZOC electrodes may be attributed to the carbon matrix obtained from cellulose, the appropriate quantity of C and ZnO phases in the ZOC composites, and their distinctive structure.

* Corresponding author. Institute of Fundamental and Applied Sciences, Duy Tan University, Ho Chi Minh City, 70000, Viet Nam.
** Corresponding author.
E-mail addresses: nguyentuanloi@duytan.edu.vn (T.L. Nguyen), itkim@gachon.ac.kr (I.T. Kim).

https://doi.org/10.1016/j.heliyon.2024.e41089
Received 4 September 2024; Received in revised form 22 November 2024; Accepted 9 December 2024
Available online 9 December 2024

1. Introduction

Nanotechnology is anticipated to serve as the cornerstone of numerous technological advancements in the 21st century, coinciding with rapid economic growth. In addition, nanotechnology-driven advances are regarded as a prominent feature of the forthcoming industrial revolution. Nanocellulose is far superior to other materials in terms of environmental sustainability and versatility, and has applications in various domains, such as biological materials [1], nano composites [2], food additives [3,4], biomedical materials [5]. Among the many existing nanoparticles, metal oxide nanoparticles are considered the most promising because they exhibit unique physical, chemical, and biological properties [6]. Zinc oxide (ZnO) is an important type II–VI semiconductor owing to its notable properties, including a wide band gap (3.2 eV), high exciton binding energy (60 MeV), strong physical and chemical durability, biocompatibility, nontoxicity, high photosensitivity, and piezoelectric and pyroelectric properties. These properties make ZnO suitable for a wide range of applications, such as in solar cells, thin-film transistors, diode lasers, transparent conductive materials, and ultraviolet lasers. Recently, the photocatalytic activity of ZnO has been extensively researched [7]. Nanostructured catalysts can be immobilized on different types of support materials to avoid agglomeration [8]. Biological polymer carriers possess additional characteristics, including reusability, improved catalytic activity, high adsorption capacity, and low cost [9]. The durability, biocompatibility, and availability of nanocrystalline cellulose make it suitable for the immobilization of catalyst particles [10]. To solve the problems of the greenhouse effect and global warming. Cellulose is one of the main biomass resources which is biodegradable and non-toxic. Therefore, compared with other biomaterials, cellulose not only possesses excellent properties including high mechanical stability, good temperature stability and unique morphology. Some cellulose-based materials have been fabricated and used for electronic devices. The use of cellulose as a carbon source not only brings many economic benefits but also contributes to environmental protection. For large-scale batteries, it has opened a new direction in the future, providing a solid alternative to carbon in Li-ion batteries [11–13].

Lithium-ion batteries (LIBs), the power source for electric vehicles, portable electronics, and mobile communication devices, have garnered particular interest in the scientific and industrial domains because of their high energy density and high efficiency. Graphite is frequently utilized as the conventional electrode for anode materials in LIBs because of its reversible charging and discharging capabilities under alternating potentials and its respectable specific capacities. To address the growing need for batteries with enhanced energy density, numerous research initiatives have focused on investigating novel electrode materials or developing new nanostructures of electrode materials [14–17]. According to estimates, the theoretical capacity of zinc oxide (ZnO) is 978 mAh g^{-1}, which is greater than that of graphite (372 mAh g^{-1}) [14,18]. Consequently, zinc oxide is a promising material for the replacement of traditional graphite anodes in LIBs. However, ZnO has poor conductivity and severe capacity degradation during cycling, which hinders its application as an anode of lithium-ion batteries. Many ZnO and carbon composite materials, such as ZnO/C, have been fabricated to address the poor electrochemical performance of ZnO [19]. In a study by Gongzheng Yang et al., a novel ZnO/nanocarbon nanoframework composite was successfully synthesized with carbon and ZnO nanoparticles used as carbon and Zn sources, respectively, and it exhibited a high specific capacity of 915 mAh g^{-1} after 100 cycles [20].

As documented in previous literature, ZnO nanoparticles have been synthesized from various sources, including *Azadirachta indica, Passiflora caerulea, Aloe vera, Vitex trifolia, Trifolium pratense, Bauhinia tomentosa,* and *Cinnamomum verum* [21–28]. The antibacterial activities of these nanoparticles have also been reported. However, the process of combining ZnO with nanocellulose has not been adopted widely. In Vietnam, *Nypa fruticants* shell is considered a promising agricultural byproduct for the production of synthetic nanocellulose materials. *Nypa fruticants* shells are commonly regarded as low value materials that are primarily utilized in agriculture, fertilizer production, and as a fuel source. Currently, there are a limited number of comprehensive studies on the production of nanocellulose from the byproducts of *Nypa fruticants* shells. Therefore, in this study, cellulose from *Nypa fruticants* shells was isolated and hydrolyzed to create nanocellulose. The next step involved the synthesis of a composite material of ZnO on a nanocellulose base using a hydrothermal method. This synthesis aims to replace graphite in rechargeable LIBs, which are in great demand worldwide. Graphite is commonly used as an anode material in commercial LIBs because of its affordability, high conductivity, and the ability to easily accommodate Li^+ ions within its layered structure. However, its low capacity renders graphite unable to meet the high-density energy storage requirements of LIBs. Consequently, scientists have become interested in substituting graphite with more appropriate materials.

2. Materials and methods

2.1. Materials

Raw materials for *Nypa fruticants* were gathered from Can Tho City, Vietnam. The material was dried in a temperature-controlled oven at 80 °C for 24 h. Subsequently, the sample was ground into a fine powder. The chemicals used were zinc nitrate hexahydrate ($Zn(NO_3)_2.6H_2O$, ≥98 %), oxalic acid dihydrate ($C_2H_2O_4.2H_2O$, ≥99.5 %), ammonia solution (NH_3, 25–28 %), formic acid (HCOOH, ≥88 %), hydrogen peroxide (H_2O_2, ≥30 %), sodium hydroxide (NaOH, ≥96 %). All chemicals were procured from Xilong Scientific Co., Ltd., China, and utilized without any purification.

2.2. Cellulose extraction from Nypa fruticants shell

After the *Nypa fruticants* shells were finely ground, 5 g of the material was weighed and placed in a beaker. The material was then mixed with water in a 1:20 (w/v) ratio of material to water for 2 h at a temperature of 90 °C and speed of 400 rpm to remove dirt and

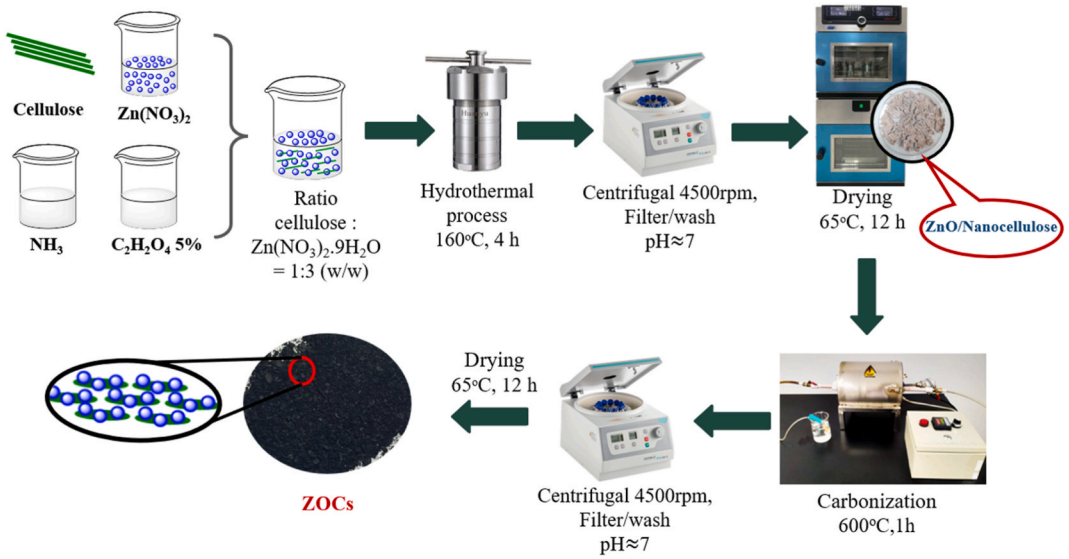

Fig. 1. Preparation of ZOCs materials.

tannins. The mixture was then filtered several times. The purified material was added to the PFA solution and subsequently stirred for 4 h at 90 °C at a speed of 400 rpm. The PFA solution was a mixture of HCOOH 90 %, H_2O_2 30 % and H_2O a volume ratio of 90:5:5 (v/v/v). The purified material and the PFA solution were mixed in a ratio of 1:40 (w/v). The obtained samples were rinsed with distilled water until the pH approached 7. Then, the samples were stirred continuously in 100 ml of 0.5 M NaOH solution for 4 h at 70 °C and rinsed again with distilled water. This step helped eliminate large amounts of lignin from *Nypa fruticants* shells. Next, the purified samples were treated with H_2O_2 30 % in a 1:4 (w/w) ratio of sample to H_2O_2. The mixture was continuously mixed for 1 h at 80 °C. When the reaction was complete, the samples were centrifuged in distilled water, and pure cellulose was finally obtained.

2.3. Synthesis of ZnO@C derived from cellulose of Nypa fruticants shell

The cellulose material obtained from the above process was impregnated with $Zn(NO_3)_2$ salt in a 1:3 (w/w) ratio of cellulose to $Zn(NO_3)_2$, combined with 20 ml of ammonia solution and oxalic acid 5 % in a 1:10 (w/v) ratio of cellulose to oxalic acid. After mixing, the mixture was put into an autoclave to perform the hydrothermal process at 160 °C for 4 h. When the hydrothermal process finished, the product was rinsed with distilled water until the pH value reached ~7 and dried in vacuum for 12 h at 65 °C. The product was pyrolyzed at 600 °C for 1, 2, and 3 h under N_2 gas. After cooling the oven to room temperature, the product was rinsed with distilled water and ethanol, dried, and ground into a fine powder. These samples were named ZOC_1h, ZOC_2h, and ZOC_3h. The synthesis process of the ZOC materials is shown in Fig. 1.

2.4. Material characterization

The structure and morphology were characterized by scanning electron microscopy (SEM, S - 4800 Hitachi) and transmission electron microscopy (TEM, Talos-F200X). The elemental distribution was studied using energy-dispersive X-ray spectroscopy (EDS). The crystal and phase structures of the ZOC samples were investigated using X-ray diffraction (XRD; Bruker ADVANCE D8). Thermal analysis was conducted using thermogravimetric analysis (TGA, TAQ500 thermal analyzer, instrument facility at the Smart Materials Research Center for IoT at Gachon University). The samples were scanned from 30 to 800 °C in ambient air.

2.5. Anode fabrication

ZOC powder (active material), super P carbon, and polyvinylidene fluoride (PVDF) were mixed at a mass ratio of 70 % for the active material, 15 % for super P carbon, and 15 % for PVDF in order to create anode electrodes. After adding a minimum quantity of N-methyl-2-pyrrolidone solvent, the mixture was stirred at 250 rpm for 24 h at room temperature in order to produce a suspension. Next, the suspension was pasted on copper foil with a doctor blade, dried at 120 °C for 4 h in a vacuum oven. The copper foils were then perforated into round shapes with a diameter of 15 mm to form the electrodes.

2.6. Electrochemical measurement

The electrochemical properties of ZOC LIBs were characterized in this study. A lithium-metal counter electrode, a reference electrode, a single layer of polypropylene film (Celgard 2400), and a ZOC working electrode were all included in each battery. The

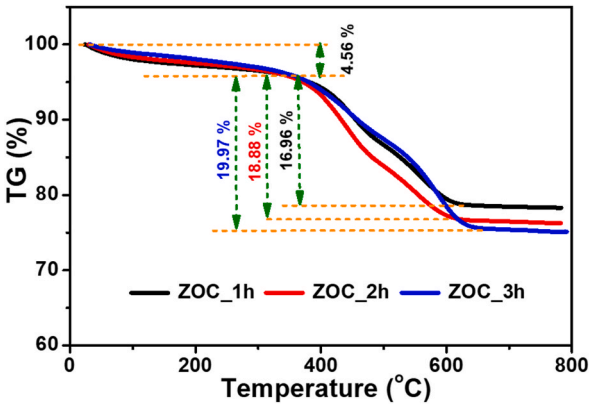

Fig. 2. TGA of ZOC samples under air atmosphere.

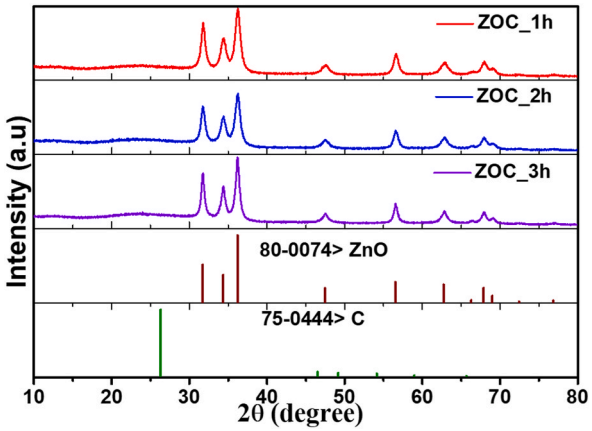

Fig. 3. The powder X-ray diffraction pattern of the ZOC samples compared to the reference peaks of ZnO and C.

electrolyte of $LiPF_6$ 1M was dissolved in a 1:1 ratio of ethylene carbonate to diethyl carbonate. The charging capacity and fast charging ability of the LIB were tested with the Neware battery testing system in the voltage range of 0.01 V–3 V (compared to Li/Li^+). Electrochemical impedance spectra (EIS) were obtained utilizing a Gamry 1010E instrument across a frequency range of 1000 kHz to 100 mHz. Cyclic voltammetry (CV) measurements were conducted utilizing the LBT20084 device from Arbin Instruments. The voltage range spanned from 0.01 V to 3 V, with a scanning speed of 0.1 mV s^{-1}.

3. Results and discussions

The carbon compositions of the ZOC_1h, ZOC_2h, and ZOC _3h samples were determined by TGA under N_2 carrier air flow passing at a speed of 40 ml/min and an air flow of 60 ml/min. The samples were heated from 30 to 800 °C at a rate of 20 °C/min. As shown in Fig. 2, the thermal degradation and stabilities of the ZOC_1h, ZOC_2h, and ZOC _3h samples were approximately identical in the early stages. All samples exhibited a weight reduction (4.56 %) as the temperature was lower than 350 °C. This loss could be attributed to moisture reduction as the water molecules in the sample began to evaporate owing to poor bonding. Between 350 °C and 650 °C, the masses of the three samples (ZOC_1h, ZOC_2h and ZOC _3h) decreased sharply by 16.96 %, 18.88 % and 19.97 %, respectively. This could be due to the reduction in the proportion of carbon in the samples. All three samples exhibited only minor mass differences in the TGA results, with ZOC_3h exhibiting a greater mass loss percentage than the other two samples. Theoretically, the carbon content in the ZOC samples will diminish with an increase in annealing duration (from 1 h to 3 h) due to the enhanced degradation of cellulose during carbonization at 600 °C under nitrogen gas. As a result, the ZOC_3h sample loses the least amount of weight when compared to the ZOC_2h and ZOC_1h samples. As illustrated in Fig. 2, the weight loss of the ZOC_3h sample surpasses that of the ZOC_2h and ZOC_1h samples. This phenomenon may be attributed to a minimal quantity of ZnO phase in the ZOC samples reacting with CO to generate Zn phase and CO_2 during carbonization, resulting in increased weight loss correlating with prolonged annealing time. Since there is only a 3 % weight loss difference between the ZOC samples, there is very little Zn phase present in the ZOC samples, making it impossible for XRD analysis to identify it. Between 650 °C and 800 °C, all three samples showed stability in material composition, with ash contents of 78.48 %, 76.56 % and 75.47 % for ZOC_1h, ZOC_2h and ZOC _3h, respectively.

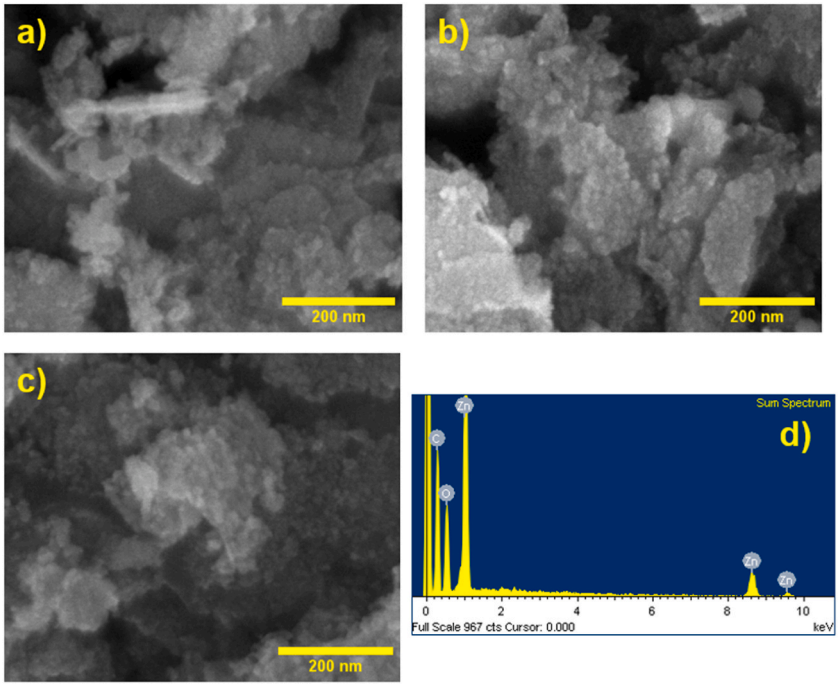

Fig. 4. SEM image of (a) ZOC_1h, (b) ZOC_2h, and (c) ZOC_3h samples. (d) EDS spectral of ZOC_2h samples.

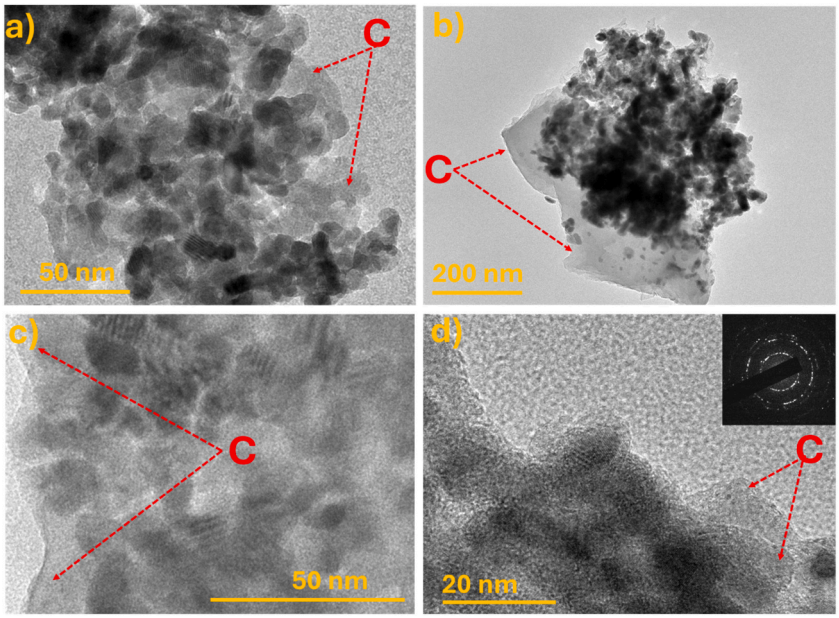

Fig. 5. TEM images of (a) ZOC_1h and (b) ZOC_3h samples. (c) TEM and (d) HRTEM and SAED images of ZOC_2h sample.

Fig. 3 shows the XRD patterns of the ZnO@C samples annealed for different durations. The peaks align well with the standard diffraction pattern of ZnO (PDF#80-0074). The XRD patterns of ZOC_1h, ZOC_2h and ZOC_3h showed high-intensity peaks at positions of 2θ angles of 31.7°, 34.4°, 36.2°, 47.5°, 56.5°, 62.7°, 67.8° and 68.9°, corresponding to the crystal orientation of (100), (002), (101), (102), (110), (103), (112) and (201). In addition, the presence of amorphous carbon was revealed by the broad peak located from 20° to 30°. This confirms the presence of both ZnO and C in the ZOC_1h, ZOC_2h, and ZOC _3h samples. By using Rietveld refinement on the XRD patterns of the ZOC samples, the structures of ZOC samples well matched the reported ZnO (PDF#80-0074) as shown in Fig. S1. In addition, the refinement results revealed that the lattice of ZOC materials was slightly enlarged when increasing annealing times

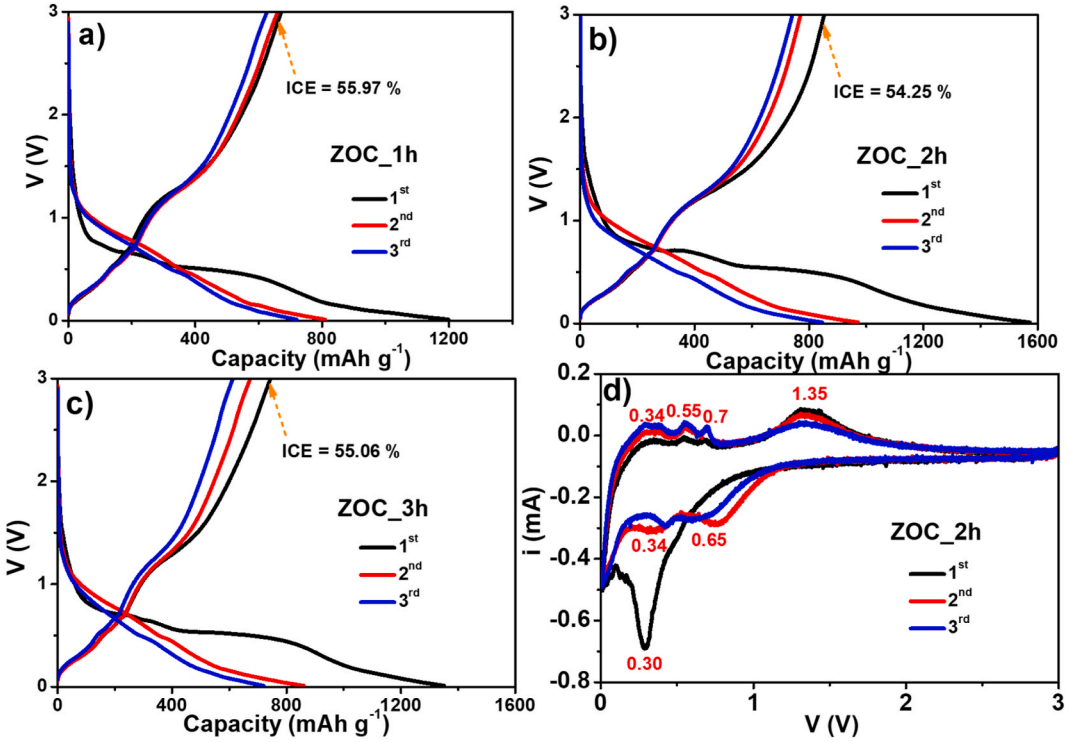

Fig. 6. Voltage profile curves of (a) ZOC_1h, (b) ZOC_2h, and (c) ZOC_3h electrodes. (d) CV curves of ZOC_2h electrode.

(Table S1).

The morphologies and elemental compositions of the ZOC_1h, ZOC_2h, and ZOC _3h samples were analyzed using SEM imaging and EDS, as shown in Fig. 4. The three samples presented nearly identical morphologies and uniform distributions of ZnO on the material surfaces, as shown in Fig. 4(a–c). However, as shown in Fig. 4(c), the particles were stacked in layers. The image clearly shows the coverage of the ZnO nanostructures on the carbon background. This structure is ideal for electrode fabrication owing to its large surface area and electrochemical properties enhancement [29]. The elemental composition of ZOC_2h was determined using EDS mapping (Fig. 4(d)). These results clearly demonstrate the uniform distribution of Zn, O, and carbon elements in the ZOC_2h sample (Fig. S2). In addition, the amount of the elements (Zn, O and C) in the ZOC_2h sample was also determined by EDS analysis as shown in Table S2. Additionally, the TEM images demonstrate the presence of ZnO nanoparticles (below 50 nm) on the surface of the carbon background in the ZOC materials, as illustrated in Fig. 5(a–c). In addition, high resolution TEM (HRTEM) and selected area electron diffraction (SAED) images (Fig. 5(d)) confirm the presence of both amorphous and crystalline phases as well as carbon background in the ZOC_2h material, which agreed well with XRD results.

Voltage profiles of the ZOC electrodes at 100 mA g^{-1} current density in the first three cycles are described in Fig. 6(a–c). These profiles exhibited nearly identical contours owing to the presence of similar active components, including C and ZnO. The ZOC electrodes annealed for 1 h, 2 h and 3 h demonstrated almost the same initial Coulombic efficiencies (ICE). However, the ZOC_1h electrode had preliminary discharging/charging capacity ratio of 1199.3/671.2 mAh g^{-1} and an ICE of 55.97 %, which were higher than the two ZOC_2h and ZOC _3h electrodes. The ZOC_2h and ZOC_3h electrodes had discharging/charging capacity ratios of 1572.6/853.2 mAh g^{-1} and 1351.6/744.2 mAh g^{-1}, respectively. The ICE values were 54.25 % and 55.06 %. Although all three electrodes exhibited low capacity values in the second and third discharging/charging cycles, the curves still matched. This proved that the capacity values were stable and that there was no sudden capacity drop. The decrease in the discharging capacity in the subsequent cycles is caused by the formation of a solid electrolyte interface (SEI) on the surface of the electrode during the first discharge. Hence, the formation of the SEI layer is an undesirable chemical reaction, but it usually occurs. Further, although the SEI reduced the battery capacity, it also helped maintain and stabilize the electrode structure second cycle onwards.

Fig. 6(d) illustrates the CV curve of the ZOC_2h electrode during the initial three cycles throughout the voltage range of 0.01 V–3.00 V, with a scanning rate of 0.1 mV s^{-1}. During the initial cathodic cycle, the broad peak observed at 0.30 V may result from the conversion of ZnO to Zn and the alloying interaction between Zn and Li^+ ions (Eq. (1) and Eq. (2)), in addition to the creation of the SEI layer [19,30,31]. A small peak occurring in the low-voltage zone (approximately 0.01 V) is thought to be associated with the C and Li^+ ion reactions (Eq. (3)) [32]. In the second and third cathodic cycles, there were two distinct peaks at 0.65 V and 0.34 V, respectively. These corresponded to the conversion of ZnO to Zn metal (Eq. (1)) and the reaction between Zn and Li^+ ions to form the Li_xZn alloy (Eq. (2)). During anode scanning, a peak in the range of 0.3 V–0.7 V and a separate peak at 1.35 V represented multi-stage oxidation [33,34]. The first peak (0.3 V–0.7 V) related to the dealloying process of Li_xZn into Zn (Eq. (4)) [35,36]. The second peak corresponded

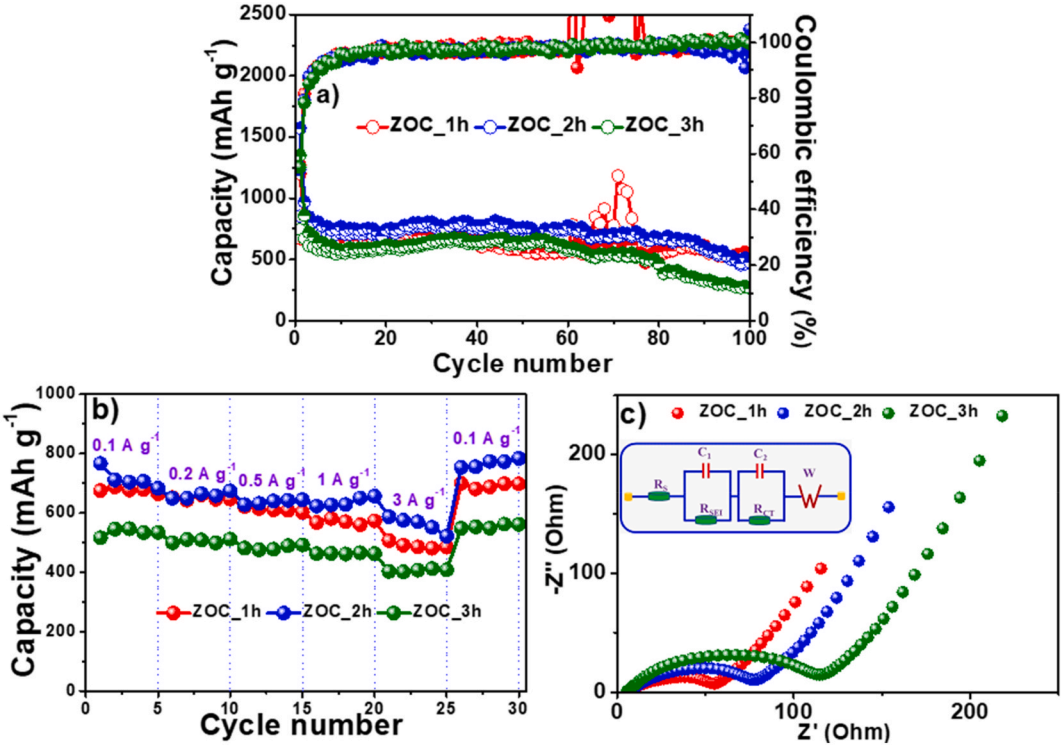

Fig. 7. (a) Cycling performance, (b) rate capacity, and (c) EIS of the ZOC electrodes.

to the oxidation of Zn to ZnO (Eq. (5)) [34,37]. Upon further cycling, the intensity of the oxidation peak at 1.35 V decreased steadily owing to the incomplete reversible oxidation of Zn to ZnO. After the initial cathodic/anodic scan, the CV curves exhibited similar shapes. This reveals stable electrochemical processes at the ZOC_2h electrodes. The CV curves of the ZOC_1h and ZOC _3h electrodes were also obtained and are shown in Fig. S3.

3.1. First discharge

$$ZnO + 2\,Li^+ + 2\,e^- \rightarrow Zn + Li_2O \quad (1)$$

$$Zn + x\,Li^+ + x\,e^- \rightarrow Li_xZn \quad (2)$$

$$C + y\,Li^+ + y\,e^- \rightarrow Li_yC \quad (3)$$

3.2. First charge

$$Li_xZn \rightarrow Zn + x\,Li^+ + x\,e^- \quad (4)$$

$$Zn + Li_2O \rightarrow ZnO + 2\,Li^+ + 2\,e^- \quad (5)$$

3.3. Subsequent discharge/charge

$$ZnO + 2\,Li^+ + 2\,e^- \leftrightarrow Zn + Li_2O \quad (6)$$

$$Zn + x\,Li^+ + x\,e^- \leftrightarrow Li_xZn \quad (7)$$

The discharging/charging capacities and Coulombic efficiencies of different cycles of the ZOC anodes at a current density of 0.1 A g^{-1} are shown in Fig. 7(a). All the electrodes exhibited a capacity decline in the first 10 cycles and then maintained their capacity from the 10th to the 80th cycle. The capacity then decreased slightly until the 100th cycle. The ZOC_1h, ZOC_2h and ZOC _3h electrodes provided charging capacity of 534 mAh g^{-1}, 500 mAh g^{-1}, and 267 mAh g^{-1} after 100 cycles, respectively. Furthermore, the electrodes

Table 1
Evaluation of the electrochemical performance of zinc oxide-based anodes for lithium-ion batteries.

Zinc-oxide-based anode	Current density (A g^{-1})	Cycle life/end reversible capacity (cycle/mAh g^{-1})	Reference
Co-ZnO@C	0.1	50/527	[38]
CF@ZnO	0.1	300/510	[39]
ZnO@C nanospheres	0.1	50/440	[40]
ZnO@C	0.825	200/496	[41]
CZO@C	0.1	50/725	[42]
$ZnMoO_4.0.8H_2O$	0.1	50/435	[43]
ZnO-C microspheres	0.1	150/520	[44]
ZnO/C	0.1	100/212	[30]
ZOC_2h	***0.5***	***150/693***	***This work***
	0.1	***100/500***	

Table 2
EIS results of ZOC electrodes after rate capacity test.

	R_e (Ω)	R_{SEI} (Ω)	R_{CT} (Ω)
ZOC_1h	6.76	10.05	28.43
ZOC_2h	7.51	12.16	44.05
ZOC_3h	6.37	14.78	70.69

consistently exhibited a high Coulombic efficiency of nearly 100 %, signifying the effective occurrence of the reversible process within the battery. The ZOC_2h electrode demonstrated superior stability in electrochemical characteristics compared to the other two electrodes. This is due to the compositional equivalence between the C and ZnO phases and the carbon matrix in the ZOC_2h sample. To investigate the effects of the annealing temperatures to the electrochemical performances, samples with a sintering time of 2 h at 500 °C and 700 °C (marked as ZOC_2h_500C and ZOC_2h_700C) were also prepared. XRD analysis of the ZOC_2h_500C and ZOC_2h_700C samples (Fig. S4a) indicated that these materials also included ZnO (PDF# 80-0074) and C (PDF# 75–0444) phases. However, the electrochemical properties of ZOC_2h_500C and ZOC_2h_700C electrodes, as shown in Fig. S4b, were inferior to those of ZOC_2h electrode. The reasons could be related to the different amount between ZnO and C phases in these samples at different annealing temperatures.

Fig. 7(b) shows the fast charging of the ZOC electrodes at different current densities. The electrodes ZOC_1h, ZOC_2h and ZOC_3h provided charging capacities of 676, 714, 535; 649, 659, 506; 611, 637, 483; 570, 636, 463; 490, 561, 406 mAh g^{-1} at current densities of 0.1, 0.2, 0.5, 1.0 and 3.0 A g^{-1}, respectively. When the current density returned to 0.1 A g^{-1}, the charging capacities were restored to 692, 768, and 554 mAh g^{-1}, respectively. The ZOC_2h electrodes displayed outstanding capacity maintenance when exposed to a high current because of the formation of a durable SEI layer and the carbon matrix from cellulose, as well as the presence of ZnO and the appropriate C phase. Obviously, the ZOC_3h electrode showed the lowest capacity at different current densities compared to the other two. These results can be related to the variation in the C and ZnO phase contents of the ZOC materials.

In addition, the cycling performances of the ZOC electrodes at a current density of 0.5 A g^{-1} were also investigated as shown in Fig. S5. The first charge capacity and ICE of the ZOC_2h electrode are 798 mAh g^{-1} and 56.2 %, respectively. Meanwhile, the ZOC_1h and ZOC_3h electrodes delivered the initial charge capacity of 453 mAh g^{-1} and 653 mAh g^{-1} with an ICE of 65.3 % and 68 %, respectively. After 150 cycles, the charge capacities of ZOC_1h, ZOC_2h, and ZOC_3h electrodes at current density of 0.5 A g^{-1} are 335 mAh g^{-1}, 693 mAh g^{-1}, and 589 mAh g^{-1}, respectively. It is noted that the ZOC_2h electrode exhibits better cycling stability at high current density compared to the ZOC_1h and ZOC_3h electrodes. The ZOC_2h anode exhibited competitive performances comparing to other zinc-oxide-based anodes, as showed in Table 1.

Electrochemical impedance spectroscopy was performed to further evaluate the differences between the ZOC anodes after the quick-charging study. The EIS profiles in Fig. 7(c) consist of two hemispheres and an elongated tail. They are correlated with the resistance of the SEI layer (R_{SEI}), charge-transfer resistance (R_{CT}), and diffusion speed of lithium ions into the anodes of the LIBs. The R_{SEI} and R_{CT} values of the ZOC_1h electrode were lower than those of the ZOC_2h and ZOC_3h electrodes in Table 2. This result corresponds to the carbon content deviation between the ZOC samples. The lower the C-content of the electrode (or the higher the ZnO content), the lower the total resistance.

The relationship between $\boldsymbol{Z'}$ and $\boldsymbol{\omega^{-0.5}}$ was linear in the Warburg region as shown in Fig. S6. The slope of these linear assigned to Warburg coefficient (σ) of the ZOC electrodes. These σ values were applied to compare the diffusion coefficient of Li^+ ions (D) value between ZOC electrodes as Arrhenius equation (Eq. S(1)). Because σ for the ZOC_1h anode (96.9 Ω $s^{-0.5}$) was lower than of ZOC_2h (135.8 Ω $s^{-0.5}$) and ZOC_3h (203.4 Ω $s^{-0.5}$), therefore, the D value for ZOC_1h was larger than of ZOC_2h and ZOC_3h ($D_{ZOC\_1h} > D_{ZOC\_2h} > D_{ZOC\_3h}$). This result also relates to the change of C-content in the ZOC samples. The lower the C-content of the electrode leads to the higher diffusion coefficient of Li^+ ions.

The CV curves of the ZOC_1h, ZOC_2h and ZOC _3h electrodes at different scanning rates in the range of 0.01 V–3.0 V were measured after two cycles of charging/discharging and are shown in Fig. 8. In Fig. 8(a–c), the CV curves of the ZOC_1h, ZOC_2h, and ZOC_3h electrodes are similar owing to the equivalent components of C and ZnO. As depicted in Fig. 8(a–c), the measurement results revealed that the peak intensity increased gradually as the scan speed rose from 0.3 mV s^{-1} to 1.2 mV s^{-1}. Using this algorithm [45,46],

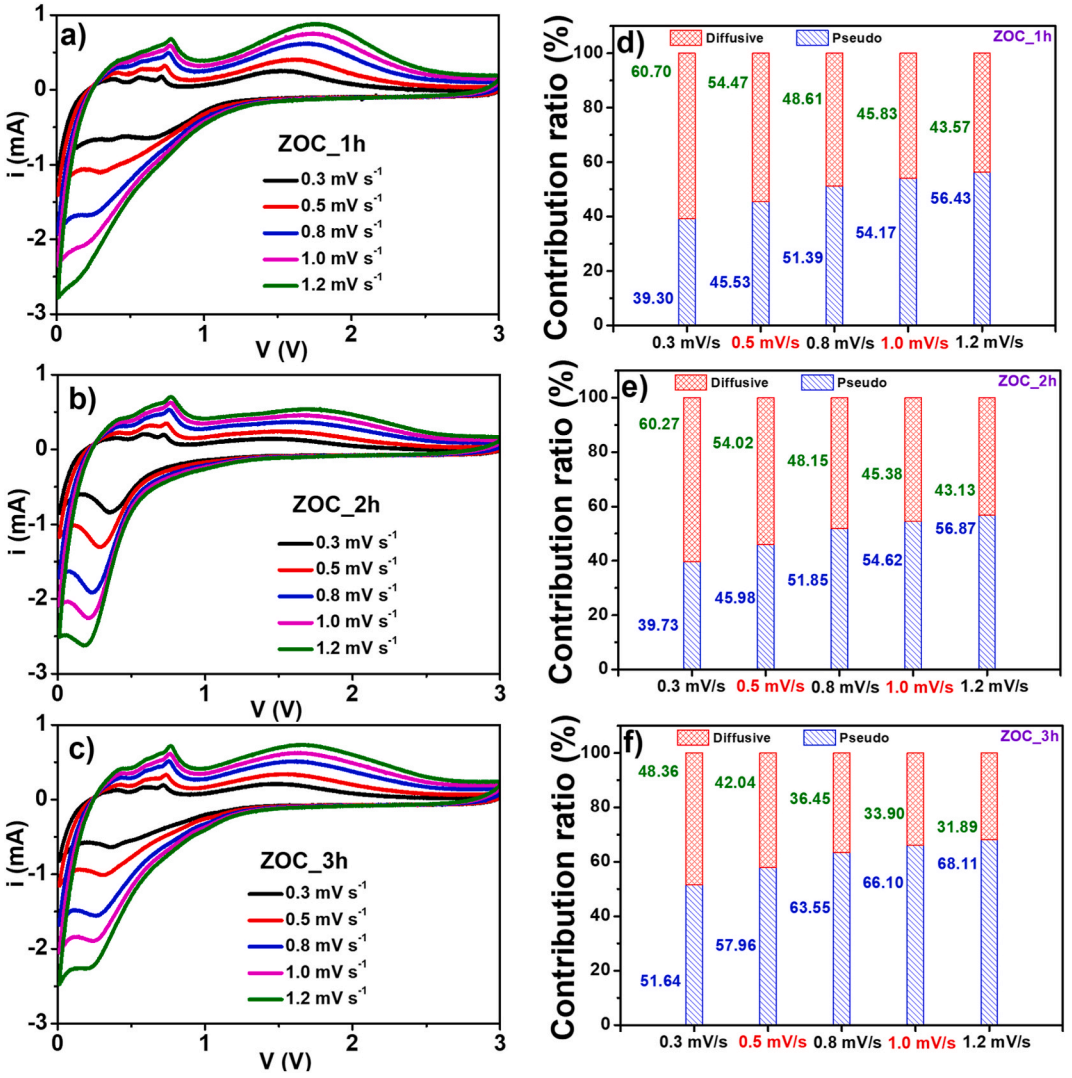

Fig. 8. (a–c) CV profiles and (d–f) contribution ratio of diffusive and pseudo behavior at various scan rates for the ZOC electrodes.

the CV curve at each scan speed could be separated into two small curves, which were equivalent to the diffusion and pseudocapacitive processes (Figure S7–9). The contribution ratio of the diffusion process and the pseudo capacitive process was evaluated based on the areas of these curves at each scan speed, and the results are shown in Fig. 8(d–f). As shown in Fig. 8(d–f), the percentage of diffusion in three samples declined as the scan speed increased from 0.3 mV s^{-1} to 1.2 mV s^{-1}. At the same scanning rate, the ZOC_3h electrode presented the highest percentages of pseudo-capacitance, and lowest value in the ZOC_1h. This result was in good agreement with the variation in the carbon content of the ZOC samples. Among the three ZOC materials, ZOC_3h had the highest carbon content, and ZOC_1h had the lowest. The samples at scanning speeds between 0.8 mV s^{-1} and 1.2 mV s^{-1} revealed that the percentage of pseudo capacity was always higher than that of the diffusion. This demonstrates the excellent ability of rapid electrode discharging/charging capacity at high current densities, which is consistent with the rate–capacity results.

4. Conclusions

In summary, a facile method was developed to fabricate ZnO@C composites from $Zn(NO_3)_2$ salts and *Nypa fruticans* shell-derived cellulose. The characterization results confirmed the presence of ZnO nanoparticles on the carbon surface, the importance of C and ZnO equivalence, and the influence of annealing on the electrochemical properties of the composites. The most suitable annealing condition was at 600 °C for 2 h in N_2 atmosphere. The composite prepared under these conditions (ZOC_2h) exhibited excellent electrochemical properties, such as a high reversible capacity and stable cycling performance. These results could be attributed to (i) the carbon matrix from the cellulose of *Nypa fruticans* shell acting as the buffering agent and conducting medium for the electrochemical reactions, thereby preventing the volume expansion of the electrode during cycling, (ii) the appropriate amount of ZnO and C (80 % ZnO and 20

% C), and (iii) the unique structure of the composite. In addition, the ZnO@C anodes in this study could be considered an excellent substitute for graphite in commercial LIBs.

CRediT authorship contribution statement

Quang Quoc Viet Thieu: Methodology, Investigation. **Thi Hoang Thy Tran:** Investigation. **Hai Dang Ngo:** Writing – original draft. **Liem Thanh Pham:** Resources, Methodology. **Man Van Tran:** Resources, Formal analysis. **Ngoc Quang Tran:** Resources, Formal analysis. **Nguyen Phuc Thien Le:** Software. **Dinh Quan Nguyen:** Visualization, Validation. **Tuan Loi Nguyen:** Writing – review & editing, Writing – original draft, Supervision. **Il Tae Kim:** Writing – review & editing, Writing – original draft, Validation, Conceptualization.

Data availability

The data supporting the findings of this study are available from the corresponding author upon reasonable request.

Declaration of competing interest

The authors declare the following financial interests/personal relationships which may be considered as potential competing interests:The authors declare the following financial interests/personal relationships which may be considered as potential competing interests:Il Tae Kim reports a relationship with Heliyon that includes: board membership.

Acknowledgments

This research is funded by the Ministry of Education and Training of Vietnam under grant number B2023-TCT-04. We acknowledge Ho Chi Minh City University of Technology (HCMUT), VNU-HCM for supporting this study.

Appendix A. Supplementary data

Supplementary data to this article can be found online at https://doi.org/10.1016/j.heliyon.2024.e41089.

References

[1] C. Zinge, B. Kandasubramanian, Nanocellulose based biodegradable polymers, Eur. Polym. J. 133 (2020) 109758, https://doi.org/10.1016/j.eurpolymj.2020.109758.
[2] R. Kumar, S. Kumari, B. Rai, R. Das, G. Kumar, Effect of nano-cellulosic fiber on mechanical and barrier properties of polylactic acid (PLA) green nanocomposite film, Mater. Res. Express 6 (2019) 125108, https://doi.org/10.1088/2053-1591/ab5755.
[3] J. Lopez-Polo, A. Silva-Weiss, M. Zamorano, F. Osorio, Humectability and physical properties of hydroxypropyl methylcellulose coatings with liposome-cellulose nanofibers: food application, Carbohydr. Polym. 231 (2020) 115702, https://doi.org/10.1016/j.carbpol.2019.115702.
[4] L. Marchetti, B. Muzzio, P. Cerrutti, S.C. Andrés, A. Califano, Bacterial nanocellulose as novel additive in low-lipid low-sodium meat sausages. Effect on quality and stability, Food Struct. 14 (2017) 52–59, https://doi.org/10.1016/j.foostr.2017.06.004.
[5] R. Curvello, V.S. Raghuwanshi, G.J. Garnier, Engineering nanocellulose hydrogels for biomedical applications, Adv. Colloid Interface Sci. 267 (2019) 47–61, https://doi.org/10.1016/j.cis.2019.03.002.
[6] W. Ahmad, D. Kalra, Green synthesis, characterization and anti microbial activities of ZnO nanoparticles using Euphorbia hirta leaf extract, J. King Saud Univ. Sci. 32 (2020) 2358–2364, https://doi.org/10.1016/j.jksus.2020.03.014.
[7] H. Morkoç, Ü. Özgür, Zinc Oxide: Fundamentals, Materials and Device Technology, John Wiley & Sons, 2008.
[8] A. Hassani, R.D.C. Soltani, S. Karaca, A. Khataee, Preparation of montmorillonite–alginate nanobiocomposite for adsorption of a textile dye in aqueous phase: isotherm, kinetic and experimental design approaches, J. Ind. Eng. Chem. 21 (2015) 1197–1207, https://doi.org/10.1016/j.jiec.2014.05.034.
[9] M. Du, Y. Du, Y. Feng, K. Yang, X. Lv, N. Jiang, Y. Liu, Facile preparation of BiOBr/cellulose composites by in situ synthesis and its enhanced photocatalytic activity under visible-light, Carbohydr. Polym. 195 (2018) 393–400, https://doi.org/10.1016/j.carbpol.2018.04.092.
[10] M. Safari, A. Khataee, R.D.C. Soltani, R.J. Rezaee, Ultrasonically facilitated adsorption of an azo dye onto nanostructures obtained from cellulosic wastes of broom and cooler straw, J. Colloid Interface Sci. 522 (2018) 228–241, https://doi.org/10.1016/j.jcis.2018.03.076.
[11] L. Jabbour, R. Bongiovanni, D. Chaussy, C. Gerbaldi, D. Beneventi, Cellulose-based Li-ion batteries: a review, Cellulose 20 (2013) 1523–1545, https://doi.org/10.1007/s10570-013-9973-8.
[12] L. Zhou, F. Pan, S. Zeng, Q. Li, L. Bai, Y. Liu, Y. Nie, Ionic liquid assisted fabrication of cellulose-based conductive films for Li-ion battery, J. Appl. Polym. Sci. 137 (2020) 49430, https://doi.org/10.1002/app.49430.
[13] S. Zhang, W. He, X. Zhang, G. Yang, J. Ma, X. Yang, X. Song, Fabricating Fe_3O_4/Fe/biocarbon fibers using cellulose nanocrystals for high-rate Li-ion battery anode, Electrochim. Acta 174 (2015) 1175–1184, https://doi.org/10.1016/j.electacta.2015.06.098.
[14] M.O. Guler, T. Cetinkaya, U. Tocoglu, H. Akbulut, Electrochemical performance of MWCNT reinforced ZnO anodes for Li-ion batteries, Microelectron. Eng. 118 (2014) 54–60, https://doi.org/10.1016/j.mee.2013.12.029.
[15] R.C.K. Reddy, J. Lin, Y. Chen, C. Zeng, X. Lin, Y. Cai, C. Su, Progress of nanostructured metal oxides derived from metal–organic frameworks as anode materials for lithium–ion batteries, Coord. Chem. Rev. 420 (2020) 213434, https://doi.org/10.1016/j.ccr.2020.213434.
[16] Y. Huang, Y. Fang, X.F. Lu, D. Luan, X. Lou, Co_3O_4 hollow nanoparticles embedded in mesoporous walls of carbon nanoboxes for efficient lithium storage, Angew. Chem. 132 (2020) 20086–20090, https://doi.org/10.1002/ange.202008987.
[17] S.L. Zhang, B.Y. Guan, H.B. Wu, X.W.D. Lou, Metal–organic framework-assisted synthesis of compact Fe_2O_3 nanotubes in Co_3O_4 host with enhanced lithium storage properties, Nano-Micro Lett. 10 (2018) 1–9, https://doi.org/10.1007/s40820-018-0197-1.
[18] J.L. Niu, C.H. Zeng, H.J. Peng, X.M. Lin, P. Sathishkumar, Y.P. Cai, Formation of N-doped carbon-coated ZnO/$ZnCo_2O_4$/$CuCo_2O_4$ derived from a polymetallic metal–organic framework: toward high-rate and long-cycle-life lithium storage, Small 13 (2017) 1702150, https://doi.org/10.1002/smll.201702150.

[19] P. Li, Y. Liu, J. Liu, Z. Li, G. Wu, M. Wu, Facile synthesis of ZnO/mesoporous carbon nanocomposites as high-performance anode for lithium-ion battery, Chem. Eng. J. 271 (2015) 173–179, https://doi.org/10.1016/j.cej.2015.02.077.
[20] G. Yang, H. Song, H. Cui, Y. Liu, C. Wang, Ultrafast Li-ion battery anode with superlong life and excellent cycling stability from strongly coupled ZnO nanoparticle/conductive nanocarbon skeleton hybrid materials, Nano Energy 2 (2013) 579–585, https://doi.org/10.1016/j.nanoen.2013.06.013.
[21] D.T. Handago, E.A. Zereffa, B.A. Gonfa, Effects of Azadirachta indica leaf extract, capping agents, on the synthesis of pure and Cu doped ZnO-nanoparticles: a green approach and microbial activity, Open Chem. 17 (2019) 246–253, https://doi.org/10.1515/chem-2019-0018.
[22] M.J. Haque, M.M. Bellah, M.R. Hassan, S. Rahman, Synthesis of ZnO nanoparticles by two different methods & comparison of their structural, antibacterial, photocatalytic and optical properties 1 (2020) 010007, https://doi.org/10.1088/2632-959X/ab7a43.
[23] J. Santhoshkumar, S.V. Kumar, S. Rajeshkumar, Synthesis of zinc oxide nanoparticles using plant leaf extract against urinary tract infection pathogen, Resource-Efficient Technologies 3 (2017) 459–465, https://doi.org/10.1016/j.reffit.2017.05.001.
[24] A. Chaudhary, N. Kumar, R. Kumar, R.K. Salar, Antimicrobial activity of zinc oxide nanoparticles synthesized from Aloe vera peel extract, SN Appl. Sci. 1 (2019) 1–9, https://doi.org/10.1007/s42452-018-0144-2.
[25] K. Elumalai, S. Velmurugan, S. Ravi, V. Kathiravan, G.A. Raj, Bio-approach: plant mediated synthesis of ZnO nanoparticles and their catalytic reduction of methylene blue and antimicrobial activity, Adv. Powder Technol. 26 (2015) 1639–1651, https://doi.org/10.1016/j.apt.2015.09.008.
[26] R. Dobrucka, J. Długaszewska, Biosynthesis and antibacterial activity of ZnO nanoparticles using Trifolium pratense flower extract, Saudi J. Biol. Sci. 23 (2016) 517–523, https://doi.org/10.1016/j.sjbs.2015.05.016.
[27] G. Sharmila, C. Muthukumaran, K. Sandiya, S. Santhiya, R.S. Pradeep, N.M. Kumar, N. Suriyanarayanan, M. Thirumarimurugan, Biosynthesis, characterization, and antibacterial activity of zinc oxide nanoparticles derived from Bauhinia tomentosa leaf extract, J. Nanostruct. Chem. 8 (2018) 293–299, https://doi.org/10.1007/s40097-018-0271-8.
[28] M.A. Ansari, M. Murali, D. Prasad, M.A. Alzohairy, A. Almatroudi, M.N. Alomary, A.C. Udayashankar, S.B. Singh, S.M.M. Asiri, B.S. Ashwini, Cinnamomum verum bark extract mediated green synthesis of ZnO nanoparticles and their antibacterial potentiality, Biomolecules 10 (2020) 336, https://doi.org/10.3390/biom10020336.
[29] M. Selvakumar, D.K. Bhat, A.M. Aggarwal, S.P. Iyer, G. Sravani, Nano ZnO-activated carbon composite electrodes for supercapacitors, Physica. B Condens. Matter. 405 (2010) 2286–2289, https://doi.org/10.1016/j.physb.2010.02.028.
[30] E. Thauer, G. Zakharova, E. Andreikov, V. Adam, S. Wegener, J.-H. Nölke, L. Singer, A. Ottmann, A. Asyuda, M. Zharnikov, Novel synthesis and electrochemical investigations of ZnO/C composites for lithium-ion batteries, J. Mater. Sci. 56 (2021) 13227–13242, https://doi.org/10.1007/s10853-021-06125-4.
[31] C.-T. Hsieh, C.-Y. Lin, Y.-F. Chen, J.-S. Lin, Synthesis of ZnO@ Graphene composites as anode materials for lithium ion batteries, Electrochimi. Acta 111 (2013) 359–365, https://doi.org/10.1016/j.electacta.2013.07.197.
[32] A. Ottmann, M. Scholz, M. Haft, E. Thauer, P. Schneider, M. Gellesch, C. Nowka, S. Wurmehl, S. Hampel, R. Klingeler, Electrochemical magnetization switching and energy storage in manganese oxide filled carbon nanotubes, Sci. Rep. 7 (2017) 13625, https://doi.org/10.1038/s41598-017-14014-7.
[33] Z.-W. Fu, F. Huang, Y. Zhang, Y. Chu, Q.-Z. Qin, The electrochemical reaction of zinc oxide thin films with lithium, J. Electrochem. Soc. 150 (2003) A714, https://doi.org/10.1149/1.1570410.
[34] C.J. Pelliccione, Y. Ding, E.V. Timofeeva, C.U. Segre, In situ XAFS study of the capacity fading mechanisms in ZnO anodes for lithium-ion batteries, J. Electrochem. Soc. 162 (2015) A1935, https://doi.org/10.1149/2.1011509jes.
[35] T. Fujieda, S. Takahashi, S. Higuchi, Cycling behaviour of electrodeposited zinc alloy electrode for secondary lithium batteries, J. Power Sources 40 (1992) 283–289, https://doi.org/10.1016/0378-7753(92)80016-5.
[36] J. Wang, P. King, R. Huggins, Investigations of binary lithium-zinc, lithium-cadmium and lithium-lead alloys as negative electrodes in organic solvent-based electrolyte, Solid State Ion 20 (1986) 185–189, https://doi.org/10.1016/0167-2738(86)90212-2.
[37] M.-G. Park, G.-K. Sung, N.-E. Sung, J.-H. Kim, C.-M. Park, Partially reversible Li_2O formation in ZnO: a critical finding supporting realization of highly reversible metal oxide electrodes, J. Power Sources 328 (2016) 607–614, https://doi.org/10.1016/j.jpowsour.2016.08.053.
[38] A.K. Giri, P. Pal, R. Ananthakumar, M. Jayachandran, S. Mahanty, A.B. Panda, 3D hierarchically assembled porous wrinkled-paper-like structure of $ZnCo_2O_4$ and Co-ZnO@ C as anode materials for lithium-ion batteries, Cryst. Growth Des. 14 (2014) 3352–3359, https://doi.org/10.1021/cg500282n.
[39] Q. Han, X. Li, F. Wang, Z. Han, D. Geng, W. Zhang, Y. Li, Y. Deng, J. Zhang, S. Niu, Carbon fiber@ pore-ZnO composite as anode materials for structural lithium-ion batteries, J. Electroanal. Chem. 833 (2019) 39–46, https://doi.org/10.1016/j.jelechem.2018.11.014.
[40] Z. Bai, Y. Zhang, N. Fan, C. Guo, B. Tang, One-step synthesis of ZnO@ C nanospheres and their enhanced performance for lithium-ion batteries, Mater. Lett. 119 (2014) 16–19, https://doi.org/10.1016/j.matlet.2013.12.060.
[41] Y. Liu, Y. Li, M. Zhong, Y. Hu, P. Hu, M. Zhu, W. Li, Y. Li, A facile synthesis of core-shell structured ZnO@C nanosphere and their high performance for lithium ion battery anode, Mater. Lett. 171 (2016) 244–247, https://doi.org/10.1016/j.matlet.2016.02.112.
[42] H. Yue, Z. Shi, Q. Wang, Z. Cao, H. Dong, Y. Qiao, Y. Yin, S. Yang, MOF-derived cobalt-doped ZnO@C composites as a high-performance anode material for lithium-ion batteries, ACS Appl. Mater. Interfaces 6 (2014) 17067–17074, https://doi.org/10.1021/am5046873.
[43] J. Fei, Q. Sun, Y. Cui, J. Li, J. Huang, Sodium carboxyl methyl cellulose and polyacrylic acid binder with enhanced electrochemical properties for $ZnMoO_4{\cdot}0.8$ H_2O anode in lithium ion batteries, J. Electroanal. Chem. 804 (2017) 158–164, https://doi.org/10.1016/j.jelechem.2017.09.061.
[44] Q. Xie, X. Zhang, X. Wu, H. Wu, X. Liu, G. Yue, Y. Yang, D.-L. Peng, Yolk-shell ZnO-C microspheres with enhanced electrochemical performance as anode material for lithium ion batteries, Electrochim. Acta 125 (2014) 659–665, https://doi.org/10.1016/j.electacta.2014.02.003.
[45] X. Pu, D. Zhao, C. Fu, Z. Chen, S. Cao, C. Wang, Y. Cao, Understanding and calibration of charge storage mechanism in cyclic voltammetry curves, Angew. Chem. Int. Ed. 60 (2021) 21310–21318, https://doi.org/10.1002/anie.202104167.
[46] N.T. Chau, H.D. Ngo, M.T. Nguyen, T.G. Tran, T.T.N. Bui, N.T. Nguyen, T.L. Nguyen, Eco-saving and green anode materials for Li-ion batteries utilizing oxide-decorated biocarbon substrates proceeded from cassava residues, Ceram. Int. 49 (2023) 39640–39648, https://doi.org/10.1016/j.ceramint.2023.09.318.